remote sensing

MDPI

Article

A Method for Convergent Deformation Analysis of a Shield Tunnel Incorporating B-Spline Fitting and ICP Alignment

Zihan Wang [1], Xiangyang Xu [1,*], Xuhui He [2], Xiaojun Wei [2] and Hao Yang [3]

[1] School of Rail Transportation, Soochow University, Suzhou 215006, China; 20214246023@stu.suda.edu.cn
[2] School of Civil Engineering, Central South University, Changsha 410075, China; xuhuihe@csu.edu.cn (X.H.); xiaojun.wei@csu.edu.cn (X.W.)
[3] School of Transportation & Civil Engineering, Nantong University, Nantong 226019, China; h.yang@ntu.edu.cn
* Correspondence: x.y.xu@suda.edu.cn

Abstract: The application of three-dimensional laser scanning technology in the field of tunnel deformation monitoring has changed the traditional measurement method. It provides an automated and intelligent solution for monitoring the geometric deformation of tunnel sections due to its high efficiency and independence from environmental influences. In this paper, based on B-spline fitting and iterative nearest point (ICP) alignment, the calculation of the difference between the radial distance and the design radius of a tunnel is transformed into a curve transformation that iterates over the nearest-neighbor points and calculates the difference in the distance between the corresponding points. The innovation of this paper is that the high-precision tunnel deformation monitoring method integrating B-spline fitting and ICP alignment can automatically compensate for the missing point clouds, is not affected by the point clouds of the tunnel inner and outer liner appendages, is more sensitive in the local deformation feedback and can be applied to a variety of tunnel shapes. The results indicate that our method maximally improves the accuracy of the horizontal convergence calculation by 28.6 mm and the accuracy of the vault settlement by 27.8 mm in comparison with the least squares circle fitting algorithm.

Keywords: 3D laser scanning technology; B-spline fitting; ICP alignment; high-precision tunnel modelling; convergent deformation

check for updates

Citation: Wang, Z.; Xu, X.; He, X.; Wei, X.; Yang, H. A Method for Convergent Deformation Analysis of a Shield Tunnel Incorporating B-Spline Fitting and ICP Alignment. *Remote Sens.* **2023**, *15*, 5112. https://doi.org/10.3390/rs15215112

Academic Editor: Riccardo Roncella

Received: 30 August 2023
Revised: 21 October 2023
Accepted: 23 October 2023
Published: 26 October 2023

Copyright: © 2023 by the authors. Licensee MDPI, Basel, Switzerland. This article is an open access article distributed under the terms and conditions of the Creative Commons Attribution (CC BY) license (https://creativecommons.org/licenses/by/4.0/).

1. Introduction

Tunnels are subject to deformation, cracks, water seepage and other disorders during prolonged operation. The real-time monitoring of geometric features of tunnel structures is of specific importance in tunnel safety monitoring projects [1]. Traditional monitoring relies on manually pre-embedding points on the target section and obtaining data with the help of equipment, such as total stations [2] or convergence meters, to assess the safety status of the tunnel. Although accurate data can be obtained from manual monitoring, it requires high time and economic costs [3]. The process of laying monitoring points is cumbersome, the cycle time is long, and the movement of the train restricts the manual operation for a long time. Therefore, there is an urgent need for an automated and intelligent monitoring means [4]. Ground-based synthetic aperture radar technology makes use of the characteristics of the reflected wave signals generated by electromagnetic waves after encountering the medium for disorder identification, and the radar transmits signals with good directionality, obtaining accurate data, but it is still necessary to deploy monitoring points on the lining [5,6]. Fiber grating technology uses the deformation of the lining to cause changes in the amplitude, frequency and wavelength of the light waves to achieve signal sensing, which allows remote and real-time monitoring, but is affected by the light intensity and the high cost of optical fiber deployment [7,8]. Infrared detection technology uses infrared temperature measurement to obtain the thermal response of the

surrounding rock, and the amount of deformation of the tunnel is determined by the combined analysis of infrared images and displacement field images. It does not need to contact the lining and has a fast-scanning speed, but is easily affected by the ambient temperature [9]. High-definition camera technology mounts a camera on a drone [10] or a mobile trolley [11] to quickly capture images of the interior of the tunnel to calculate the cross-sectional deformation of the metro tunnel, with a short cycle time for image acquisition, high efficiency but low resolution, and complex image processing algorithms. The three-dimensional (3D) laser scanning technique uses a laser scanner to obtain 3D point cloud data on the lining surface, which has the characteristics of contactless and fast scanning compared to the limitations of the techniques above and can obtain high-precision and high-resolution modelling features, with an excellent robustness of the point cloud data to changes in light and temperature [12–15]. The 3D laser scanning technology has been proved to be the most applicable method, especially in tunnel convergence and deformation analysis. Scholars have studied the application of 3D laser scanning technology in tunnel convergence deformation in depth. The processing of point clouds can be divided into model- and section-based methods.

The model-based approach analyzes the lining health status, such as central axis alignment, vault settlement and horizontal displacement, by constructing a 3D geometric model of the tunnel as a whole. Farahani, for example, constructed the tunnel model by triangulating meshed point clouds. The close connection between the point clouds causes this method to require an extremely high purity of the point clouds, and, inevitably, the point cloud information of the tunnel appendages interferes with the establishment of the topological relationship of the tunnel lining model. In addition, the triangular mesh weaving in the dense point cloud region is complicated and requires the support of hardware with high arithmetic power [16]. Cao et al., fitted a series of cross-section points by interpolation and resampled the generated cross-section points at specific rotation intervals to reduce the difficulty of model construction [17]. Compared with the triangular meshed model, the lightweight model effectively overcomes the missing data and density inconsistency with the resampling measure, ensures the topological relationship of the model and converges the deformation analysis more accurately. However, local details, such as information at bolt holes, and longitudinal and transverse seams of the tube sheet, may be lost. Concentrated stresses at bolt holes can lead to deformation or even damage of the lining, and pressures at the joints of tube sheets can lead to misalignment of the tunnel lining, both of which are not negligible [18]. Therefore, the lining block unit modelling method is proposed. Cao et al., unfolded the 3D point cloud map and segmented the lining units by identifying the lining joints, and applied the least squares method to match them with the templates in the lining block unit library and combined them into a tunnel model. Compared with the triangular gridded model and the lightweight model, the block cell model is more accurate and faster, and the missing lining areas can be recovered a priori by the structure. However, the establishment of a lining library requires extra work, and the resolution of the two-dimensional unfolding map affects the identification accuracy of lining joints and the completeness of model construction. This method is currently only applicable to circular tunnels [19].

In conclusion, the advantage of the model-based approach is that it can reflect the overall topological relationship of the tunnel and monitor the health of the whole tunnel. The efficiency of analyzing large-scale point cloud data is increasing with the rapid improvement of computer performance. However, noise points, outliers and missing regions are still a great challenge for model construction.

The constant cycle monitoring of tunnel segments can provide an effective guarantee for safe tunnel operation in engineering practice. The cross-section-based method is more efficient in data processing for long-mileage tunnels and more accurate in calculating local deformation than the model-based method because the point cloud data of the whole tunnel are divided into a series of cross-sections [20]. Therefore, the cross-section-based method is more often applied and improved. The section-based approach assesses the

lining health by extracting a series of cross-sectional planes perpendicular to the center axis of the tunnel and comparing them with the design planes. It mainly analyzes the tunnel center axis deviation, convergent deformation and misalignment [21]. The general steps of the cross-section-based method are as follows: (1) tunnel center axis extraction; (2) cross-section point cloud extraction; (3) cross-section point cloud denoising fitting; and (4) calculating the difference between the fitted cross-section and the design cross-section and plotting the deformation curve. This method is more robust to anomalous data compared with the classical parameter estimation methods, but the application scenario is limited to only linear tunnels [22]. In order to achieve the extraction of nonlinear tunnel axes, Cao et al. added the XOZ projection space based on the XOY projection space and used the system of two two-dimensional space axes to represent the three-dimensional space axes, in addition to transforming the original data space into tangent space, which simplified the difficulty of data processing. However, there is still overlapping or offset at the connection of the linear and nonlinear axes [17]. In order to smooth the tunnel axes, Yi et al. proposed circle fitting and B-spline curve approximation to the center of the cross-section circle to iterate the tunnel axes until convergence [23]. The center axis is vertically projected or interpolated according to the center axis extracted in the previous step for the extraction of the cross-section point cloud. The projection method not only simply and completely retains the information of the tunnel point cloud, but also inevitably contains a lot of noise; thus, the subsequent processing of noise is the key to the research of the projection method, and a high-quality point cloud can establish a high-precision tunnel model [24]. Compared with the projection method, the interpolation method can reduce the influence of noise on the model and has better robustness to the location of occluded or empty point clouds. However, the judgement of local deformation, such as longitudinal joint misalignment and concrete spalling under high axial compression of the tube sheet, is distorted [25]. Filters such as the radius, mean and Gaussian are commonly used for noise removal in the denoising of point clouds [26]. This is simple and efficient but not applicable to the tunnel shape. Cheng et al., proposed an angle-based filtering algorithm [27] to solve the limitations of the tunnel shape but the noise on the outside of the tunnel cannot be removed, and also removes the effective point cloud where there are local deformations. Consequently, Cui et al., designed a filtering algorithm based on the discrete wavelet transform [28], which converts the point cloud right-angle coordinates into polar coordinates and inputs them into two filters, high- and low-pass, so that it can be independent of local deformation of the tunnel shape and can take into account both the noise inside and outside of the tunnel [28]. Wang et al., further researched and subdivided the categories of the noise into the tunnel lining-affiliated point cloud and outliers generated by scanner reflections, and applied a Euclidean clustering algorithm to remove the noise while preserving the geometric features of the tunnel intact [29]. In terms of tunnel cross-section curve fitting, Xu et al., applied the Random Sample Consensus (RANSAC) algorithm to fit the model parameters of a circular cross-section of a tunnel [30]. Xie et al., concluded that the cross-section of a tunnel is more in line with elliptical characteristics rather than a circle when the tunnel is under the influence of inhomogeneous subsurface stresses, and, therefore, the RANSAC algorithm estimates five parameters of an ellipse. Fitting the cross-section using regular geometry tends to lead to model errors and some nonlinear deformations are masked [31]. For this reason, Yang et al., proposed achieving the best approximation of the tunnel cross-section model using B-spline estimation [4] and verified that the B-spline free curves match the laser tracker results using the Bayesian information criterion [32]. Regarding the calculation of convergent deformation values, mostly for circular tunnels, the point deformation of the tunnel is measured by comparing the radial distance with the design radius of the tunnel section, which is obtained from the distance between the center of the circle and the cross-section point obtained by a circle or ellipse fitting algorithm [33–35]. Few studies have been carried out on tunnel shapes such as rectangular-like and horseshoe tunnels.

Despite the research work conducted by scholars mentioned above, there are still some key issues that deserve further investigation. The a priori compensation at the missing

places of the point cloud, the removal of noise to retain the integrity of the deformation information, the tunnel curve fitting to be sensitive to local deformation, and the convergent deformation calculation to be applicable to various tunnel shapes are some examples. In this paper, based on the principles of B-spline fitting and Iterative Closest Point (ICP) alignment, the problem of comparing the radial distance of the tunnel with the design radius is transformed into a curve transformation iterative nearest-neighbor problem. A high-precision modelling method is proposed for the purpose that automatically compensates for the missing point clouds, is not affected by the point clouds of internal and external tunnel lining appendages, is more sensitive to local deformation detection and can be applied to various tunnel shapes.

2. Methods

The flow of the high-precision modelling method integrating B-spline fitting and ICP alignment is shown in Figure 1. The initial point cloud data are obtained by a laser scanner, and pre-processed by projection, slicing and denoising operations to obtain a relatively pure point cloud, the B-spline curve reconstructs the tunnel model to obtain the fitted point cloud data, the simulated point cloud of the tunnel design section is simulated, and the ICP alignment method is used to align the fitted cross-section cloud with the designed cross-section cloud, and the Euclidean distances between the corresponding points are calculated last, and the folding line and deformation diagrams are plotted and visualized in terms of the color gamut.

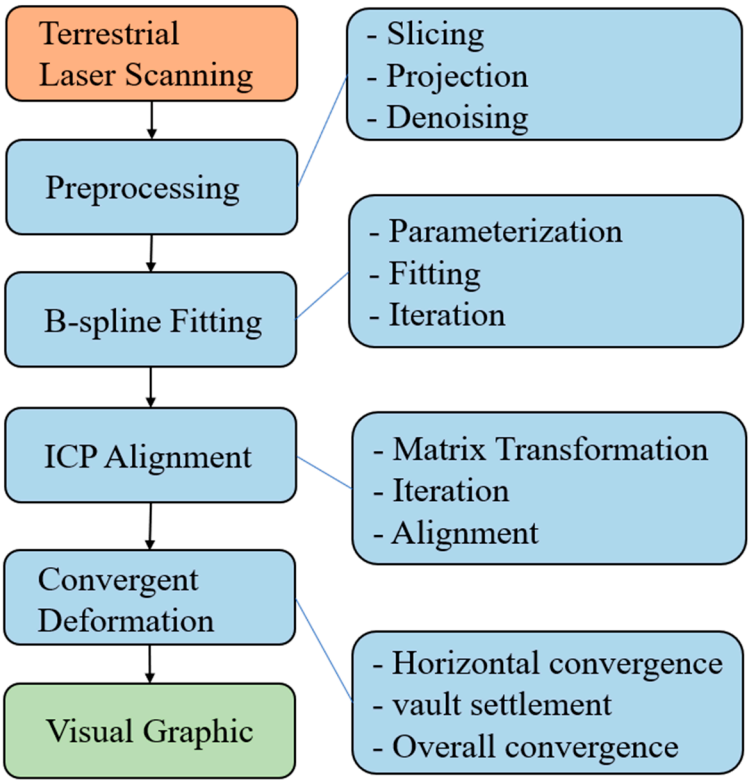


Figure 1. Algorithm flowchart.

2.1. Pre-Processing

The initial point cloud data contain interfering point clouds, such as workers, cables, tracks and tunnel lining appendages, as shown in Figure 2a. These uninteresting point clouds need to be removed to obtain a purer tunnel section point cloud to improve the fitting accuracy and computational efficiency (b).

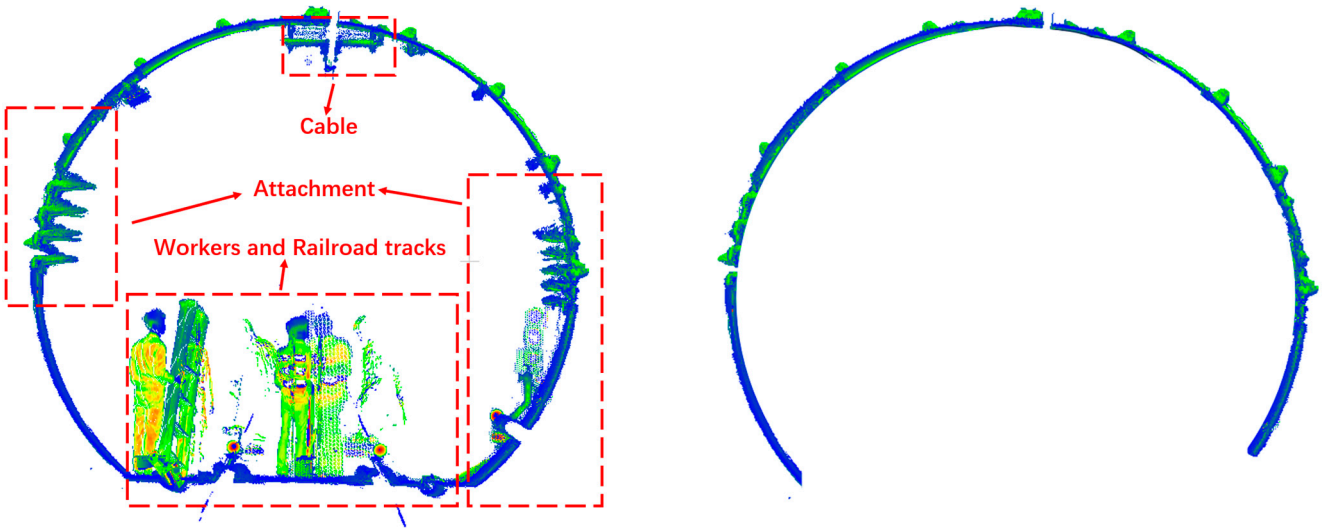


Figure 2. Initial point cloud processing. (**a**) Before processing. (**b**) After processing.

2.2. B-Spline Curve Fitting

In this paper, the best approximation of the geometric features of the tunnel cross-section is achieved by using a B-spline curve, where B(u) in Equation (1) defines the functional expression of the B-spline curve.

$$\mathrm{B(u)} = \sum_{i=0}^{n} N_{i,p}(u) C_i, u \in [0,1] \tag{1}$$

where C_i denotes the control point and the subscript i is the cyclic variable from 0 to n. Therefore, the number of control points of the B-spline curve is $n + 1$. $N_{i,p}(u)$ denotes the basis function, and the subscript p is the basis function order. The B-spline curve divides the domain of definition u into multiple node segments, as shown in Equation (2).

$$\mathrm{U} = \{0, \cdots, 0, u_{p+1}, \cdots, u_{m-p-1}, 1, \cdots, 1\}, u \in (0,1) \tag{2}$$

where U denotes the set of $m + 1$ non-decreasing nodes and the value of m is determined by the relation $m = n + p + 1$. The basis function $N_{i,p}(u)$ is defined by the Cox–deBoor recursion formula [36,37], as shown in Equation (3). Notably, the zero-order basis function $\mathrm{N}_{i,0}(u)$ is equal to 1 in the nodal interval $[u_i u_{i+1})$, and outside this interval, it is equal to 0. For a more detailed description of the mathematical representation of the B-spline curve, see the standard literature [38–40].

$$\mathrm{N}_{i,0}(u) = \begin{cases} 1 & \text{if} \quad u_i \le u < u_{i+1} \\ 0 & \text{otherwise} \end{cases}$$

$$\mathrm{N}_{i,p}(u) = \frac{u - u_i}{u_{i+p} - u_i} N_{i,p-1}(u) + \frac{u_{i+p+1} - u}{u_{i+p+1} - u_{i+1}} N_{i+1,p-1}(u) \tag{3}$$

As shown in Figure 3, the red points represent the control points and the blue curve represents the B-spline curve, which (a) can reconstruct the tunnel curve model excellently when there is no local deformation, and (b) can extract the geometrical features of the tunnel cross-section more accurately by taking advantage of the high degree of freedom of the B-spline curve. When there is a local deformation of the tunnel curve, the position of the control points will be changed sensitively and, thus, lead to the change in the trend of the B-spline curve. In the previous study, the values of B-spline parameters n and p were investigated based on the mean square deviation, and the B-spline performs best in terms

of accuracy, robustness and computing speed when n = 3 and p = 10; the specific research process is shown in [41].

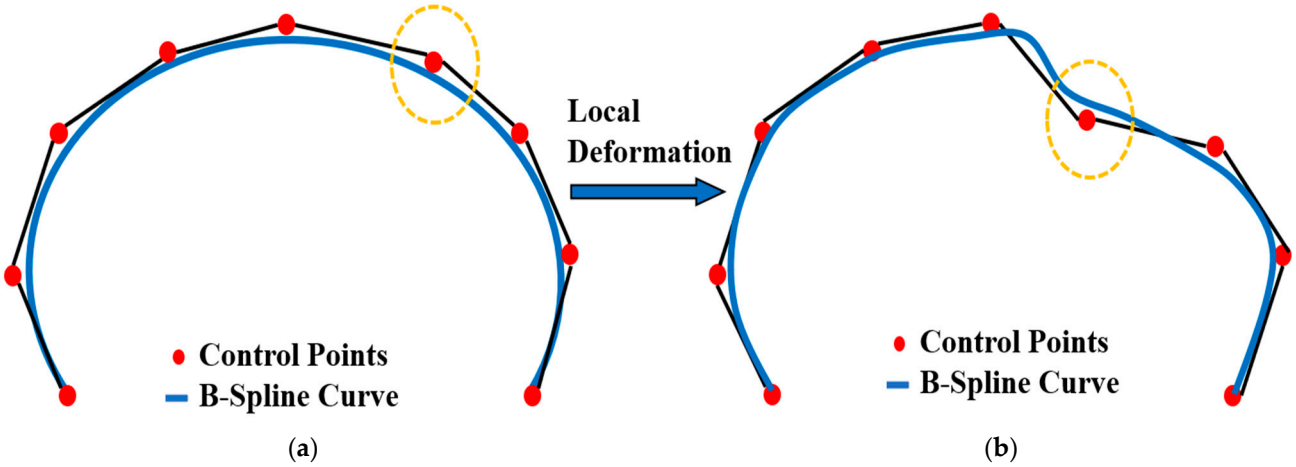


Figure 3. Schematic of B-spline fitting. (**a**) Without local deformation. (**b**) With local deformation.

2.3. ICP Alignment

The ICP algorithm proposed by Besl and Mckay [42] is essentially an optimal matching of two sets of point cloud data in different coordinate systems under satisfying the metric criterion through certain rotation and translation transformations. Defining the source point cloud as S and the target point cloud as T, the Euclidean distance calculation function E_k between S and T in the kth iteration is shown in Equation (4).

$$E_k(\boldsymbol{R_k}, \boldsymbol{V_k}) = \frac{1}{n} \sum_{i=1}^{n} \| \left(\boldsymbol{R_k} S_{(k-1)i} + \boldsymbol{V_k} - T_i\right) \|^2 \tag{4}$$

where n denotes the number of source point clouds, S_k is the update S after k iterations (S_0 is the source point cloud), S_{ki} represents the ith point in S_k, and T_i represents the nearest point in T corresponding to the point S_i. $\boldsymbol{R_k}$ denotes the rotation matrix and $\boldsymbol{V_k}$ denotes the translation vector as shown in Equation (5).

$$\boldsymbol{R_k} = \begin{bmatrix} \boldsymbol{\cos\beta} & \boldsymbol{\sin\beta} \\ \boldsymbol{-\sin\beta} & \boldsymbol{\cos\beta} \end{bmatrix}_k \tag{5}$$

$$\boldsymbol{V_k} = \left(\boldsymbol{V_x}, \boldsymbol{V_y}\right)^{\boldsymbol{T}}_{\boldsymbol{k}} \tag{6}$$

In this paper, the point cloud of the B-spline fitting curve is the source point cloud S, and the point cloud of the circular tunnel design section is the target point cloud T. As shown in Figure 4, the red curve indicates the circular tunnel design section, the blue curve indicates the B-spline fitting curve, the dashed line of the S_0 is the source point cloud that indicates the curve after the matrix transformation, the optimal correspondence between S and T is determined after k iterations, and the distance between the corresponding points is calculated to be the required converged deformation value of the tunnel. The out-of-circle displacement is defined as positive, and the in-circle displacement is defined as negative. The maximum positive displacement reflects the horizontal convergence, the maximum negative displacement reflects the settlement of the arch, and the root mean square of displacement reflects the overall convergence. Alignment is performed in the following steps [43]:

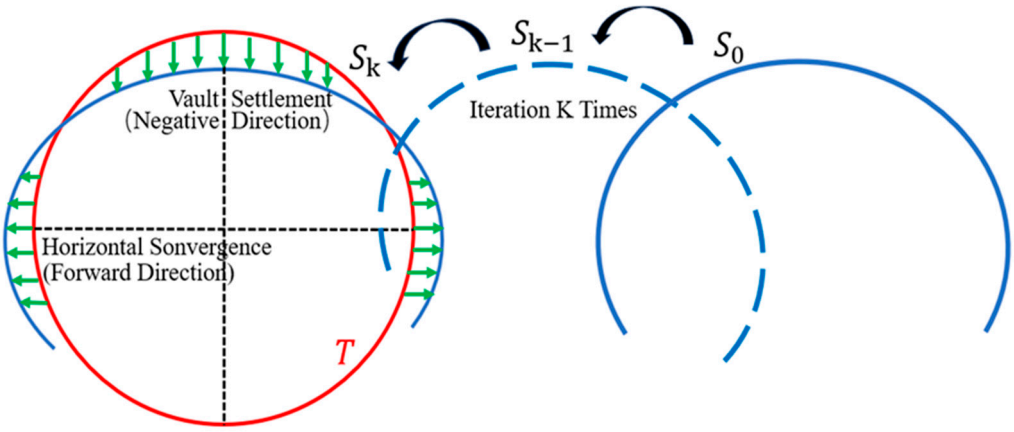


Figure 4. Deformation analysis based on the ICP alignment.

1. Calculate $\boldsymbol{R_k}$ and $\boldsymbol{V_k}$ to minimize E_k according to Equations (4)–(6).
2. Update P_k according to Equation (7). Third item.

$$S_k = R_k \cdot S_{k-1} + \boldsymbol{V_k} \tag{7}$$

3. Replace $S_{(k-1)}$ with S_k in Equation (4).
4. Determine the correspondence between the final S and T. Calculate the convergent deformation $D(S_i, T_i)$ at each point of the tunnel cross-section according to the Euclidean distance Equation (8). Calculate the overall convergent deformation $D_{RMS}(S_i, T_i)$ of the tunnel cross-section according to the root mean square Equation (9).

$$D(S_i, T_i) = \sqrt{\left(x_{(S_i)} - x_{(T_i)}\right)^2 + \left(y_{(S_i)} - y_{(T_i)}\right)^2} \tag{8}$$

$$f = D_{RMS}(S_i, T_i) = \sqrt{\frac{\sum_{i=1}^{n} D(S_i, T_i)^2}{n}} \tag{9}$$

5. Repeat steps 1–4 and the iteration stops when the objective f_{min} is satisfied according to Equation (9).

2.4. Comparison of Method

A comparison is made with the traditional circle fitting method to validate the advantages of the high accuracy tunnel deformation monitoring method incorporating B-spline fitting and ICP alignment. The least squares circle fitting algorithm in Equation (10) can be described by the center and radius of the circle, where the circle radius R is a fixed value and (x_i, y_i) are the pre-processed point cloud coordinates. The optimal solution circle center coordinates (x_M, y_M) are obtained when the objective function f_{min} is satisfied. The convergence deformation of each point of the tunnel cross-section is calculated according to the Euclidean distance Equation (11). We can calculate the overall convergent deformation $D_{RMS}(x_i, y_i)$ of the tunnel cross-section according to the root mean square Equation (12). The out-of-circle displacement is specified as positive and the in-circle displacement as negative. The maximum positive displacement reflects the horizontal convergence, the maximum negative displacement reflects the vault settlement, and the root mean square of displacement reflects the overall convergence.

$$(x_i - x_M)^2 + (y_i - y_M)^2 - R^2 = 0 \tag{10}$$

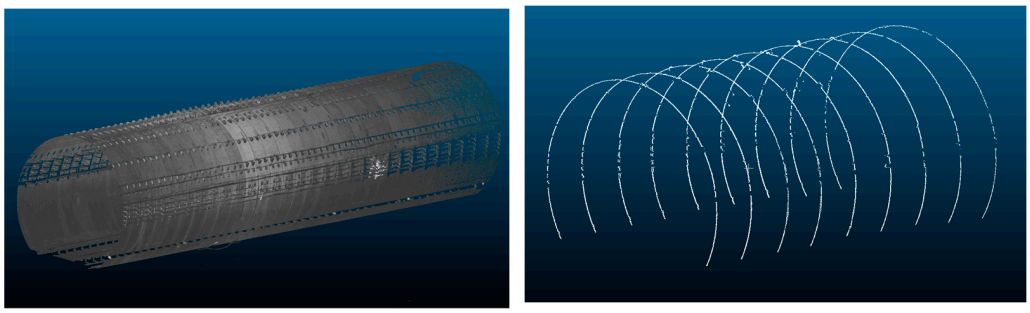
$$D(x_i, y_i) = \sqrt{(x_i - x_M)^2 + (y_i - y_M)^2} - \mathrm{R} \tag{11}$$

$$f = D_{RMS}(x_i, y_i) = \sqrt{\frac{\sum_{i=1}^{n} D(x_i, y_i)^2}{n}} \tag{12}$$

3. Results

3.1. Data Selection

In this paper, the point cloud of a 48 m long 5.5 m diameter circular tunnel was collected by a laser scanner, as shown in Figure 5. Firstly, the point cloud data are pre-processed, cut into eight groups of lined pipe rings according to a width of 6 m and projected on the XOZ plane. The workers, cables, tracks and tunnel lining appendages and other interfering point clouds are then removed to obtain the eight purer groups of tunnel cross-sectional point clouds. The number of the eight groups of tunnel cross-section point clouds is shown in Table 1, and the closer the cross-section of the point cloud to the site of the laser scanner, the denser it is.



(**a**) (**b**)

Figure 5. The 3D point cloud of the tunnel. (**a**) Initial point cloud of the tunnel. (**b**) Pre-processed point cloud of the tunnel section.

Table 1. Summary of the number of cross-sections point clouds.

Section ID	1	2	3	4	5	6	7	8
Number	2045	3741	5819	6779	6495	7249	7156	10,695

The tunnel design section relies on MATLAB to automatically generate and uniformly sample a circular model with a diameter of 5.5 m. The number of point clouds of the design section is approximated to the cross-section collected by the laser scanner. There is no noise interference in the design section, so it has no impact on the experimental results.

3.2. Experimental Results

Eight groups of tunnel cross-section point clouds are calculated by a least squares circle fitting algorithm and our algorithm, respectively, for horizontal convergence, vault settlement, and overall convergence. The results are shown in Table 2, with positive and negative representing the direction, the least squares circle fitting algorithm needs to obtain the optimal solution center of the circle coordinates, and our method does not need to obtain the center of circle coordinates. It is significant that our method is robust to the density of point clouds.

3.3. Deformation Visualization

A visual deformation map by a color field is plotted, as shown in Figure 6, to qualitatively demonstrate the deformation of the tunnel cross-section. The black curve is the design model of the tunnel with a radius of 2.75 m. The colored curve is the curve model drawn by the degree of convergent deformation after B-spline fitting and alignment with the design model. In order to quantitatively demonstrate the results of the circle fitting algorithm and our algorithm's displacement calculations for each cross-section point cloud,

convergent deformation line graphs are plotted, as shown in Figure 7, where the blue curves are the results of the least squares circle fitting algorithm, and the orange curves are the results of our algorithm. Our algorithm has similar but smoother deformation curve trends compared to the least squares circle fitting algorithm.

Table 2. List of comparative analyses between circular fitting and our method.

Section ID	Method	Coordinates of the Center of the Circle	Horizontal Convergence/m	Vault Settlement/m	Overall Convergence/m
1	Circular fitting	(12.0149, 0.0015)	0.1985	−0.0560	0.0940
	Ours	/	0.1736	−0.0645	0.0941
2	Circular fitting	(12.3134, 0.0136)	0.1918	−0.0568	0.0930
	Ours	/	0.1790	−0.0543	0.0930
3	Circular fitting	(14.1577, −0.0280)	0.1605	−0.0515	0.0823
	Ours	/	0.1647	−0.0793	0.0835
4	Circular fitting	(12.8707, −0.0086)	0.1926	−0.0603	0.0854
	Ours	/	0.1831	−0.0512	0.0848
5	Circular fitting	(12.5944, −0.0030)	0.1827	−0.0533	0.0865
	Ours	/	0.1739	−0.0532	0.0863
6	Circular fitting	(13.1342, −0.0174)	0.1704	−0.0482	0.0774
	Ours	/	0.1701	−0.0457	0.0772
7	Circular fitting	(13.3934, −0.0313)	0.1892	−0.0375	0.0783
	Ours	/	0.1606	−0.0337	0.0781
8	Circular fitting	(13.8938, −0.0258)	0.1642	−0.0493	0.0807
	Ours	/	0.1665	−0.0489	0.0807

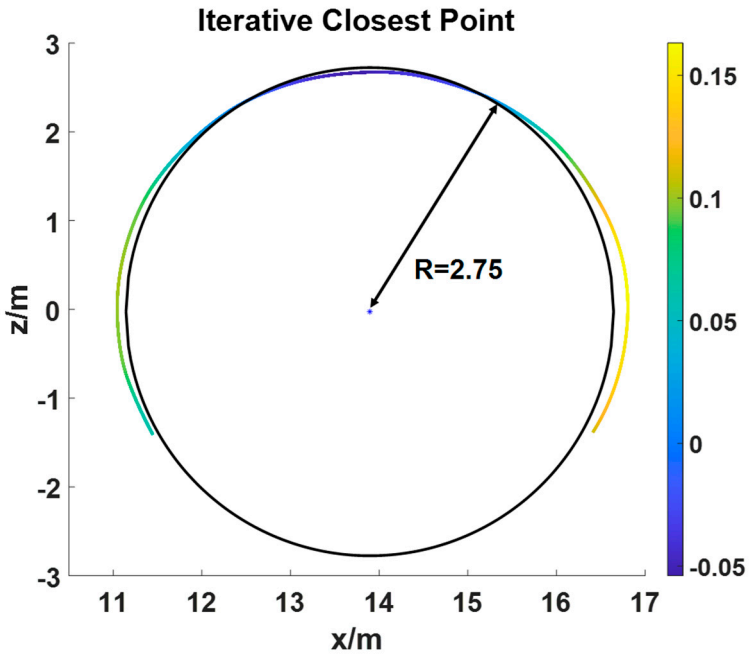


Figure 6. Visualized gamut deformation.

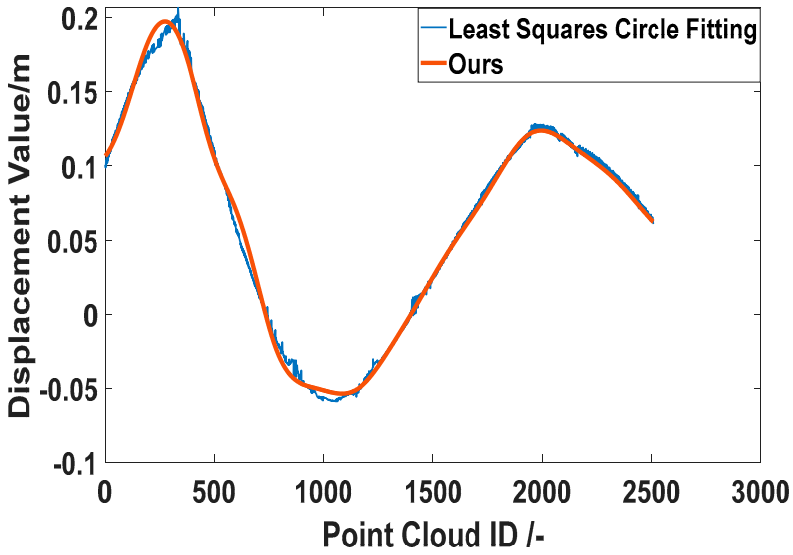


Figure 7. Cross−section point displacement.

4. Discussion

In order to further analyze the difference between the circle fitting algorithm and ours, Table 2 is classified to plot the horizontal convergence, vault settlement and overall convergence line graphs. As shown in Figure 8, the positive and negative represent the direction, where the blue curve is the result of the least squares circle fitting algorithm, and the orange curve is our result. The overall calculation result of our method is small compared to the least squares circle fitting algorithm in the horizontal convergence line graph (a); the overall calculation result of our method is large compared to the least squares circle fitting algorithm in the vault settlement line graph (b); and the two methods converge in the overall convergence line graph (c).

Furthermore, the advantages of our method over the least squares circle fitting algorithm are investigated. Figures 9–14 corresponding to the cross-sections 2–8 in Figure 8 show the advantages of our method over the circle fitting algorithm in detail. The black points in (a) represent the pre-processed point cloud, the green curve represents the circle-fitting tunnel cross-section, and the red curve represents the tunnel cross-section fitted by our method. The blue curve in (b) represents the converged deformation curve of the circle fitting algorithm and the orange curve represents the converged deformation curve of our method. Two different fitting results are shown in the box of (a), and, therefore, the results of point displacement calculation in the box of (b) are different.

The circle fitting algorithm, which cannot compensate for the lack of a continuous point cloud when fitting the tunnel point cloud, shows stepped burrs in the converged deformation plot in Figure 9. The circle fitting algorithm, when fitting the tunnel point cloud, cannot compensate for the long-distance point cloud missing, and this deformation is skipped in the convergent deformation map, as shown in Figure 10. Our method can effectively compensate for the continuous and long-distance point cloud missing, showing smoother deformation curves in the converged deformation map, and the neglected part can predict the corresponding deformation by the a priori knowledge. It is verified that our method calculates the higher deformations for vault settlement in cross-section 3.

The circle fitting algorithm cannot be affected by the interfering point cloud outside the tunnel lining when fitting the tunnel point cloud, as shown in Figure 11, and, thus, shows the peak-like shape of the prominent curve in the converged deformation map. Our method can effectively distinguish the interference from the appendages outside the lining, and the deformation curves do not show the peak-like error in the converged deformation map. The circle fitting algorithm removes the misplaced platforms of the lining as interfering point clouds when fitting the tunnel point clouds, as shown in Figure 12; thus, this real

deformation is ignored in the converged deformation map. Our method can effectively identify the misplaced platforms of the lining, and the deformation curve in the convergent deformation map shows a larger deformation, which can provide timely feedback on the misplacement of the lining.

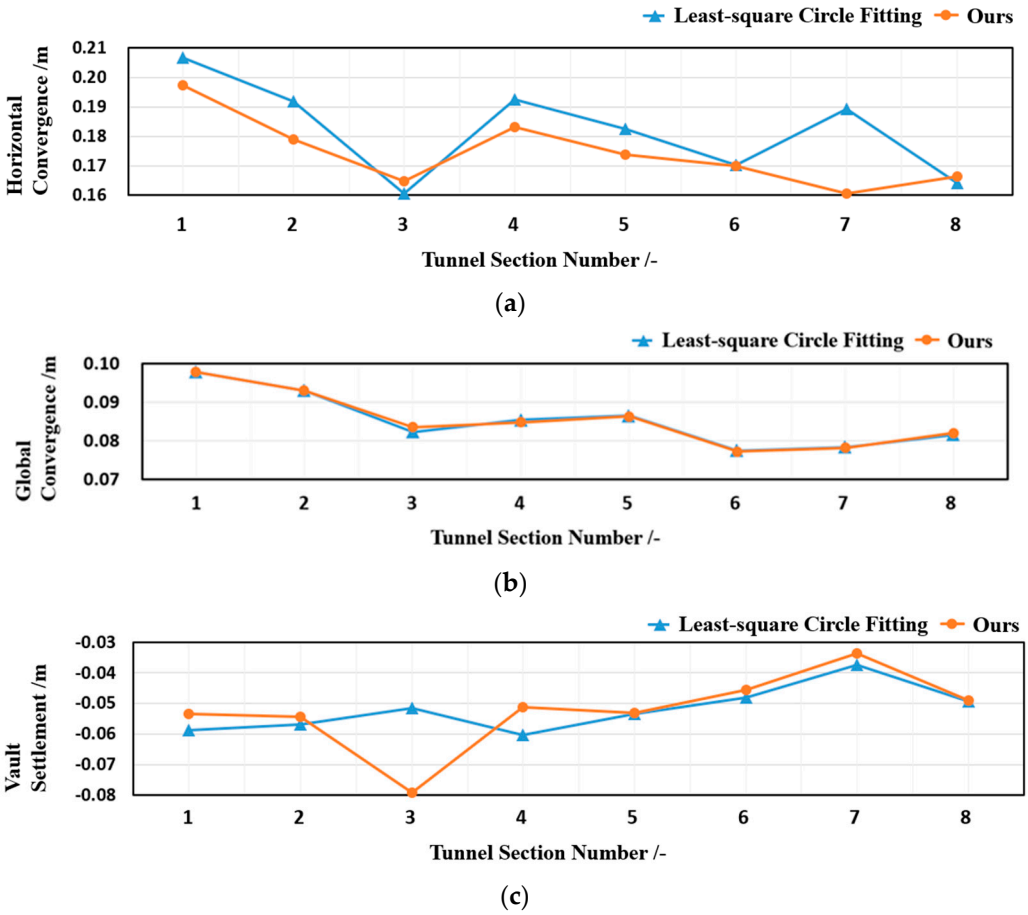


Figure 8. Line graph of the convergent deformation of the cross−section. (**a**) Horizontal convergence. (**b**) Vault settlement. (**c**) Overall convergence.

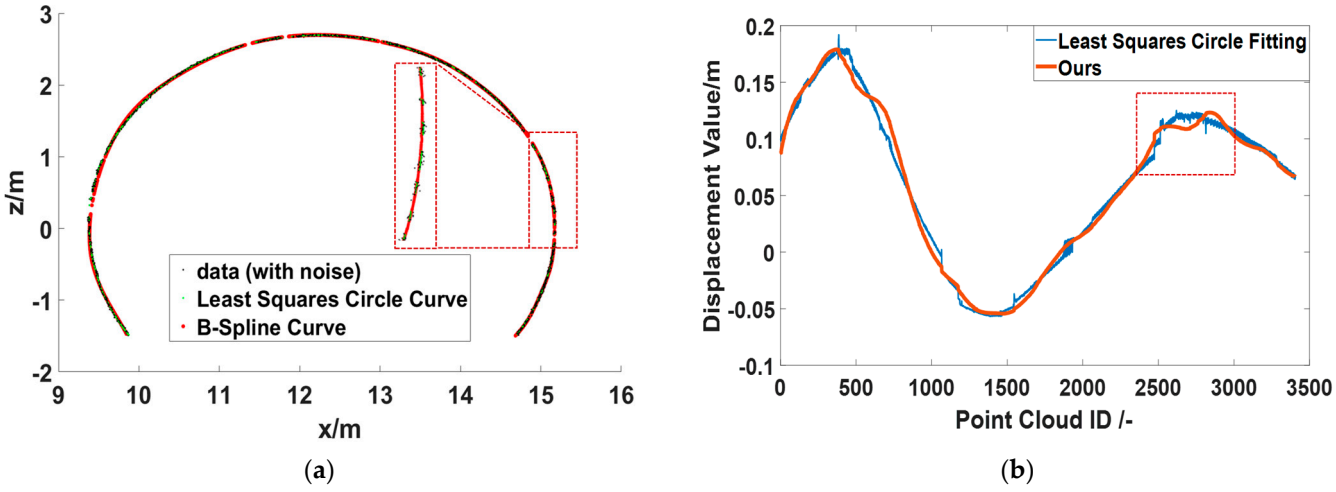
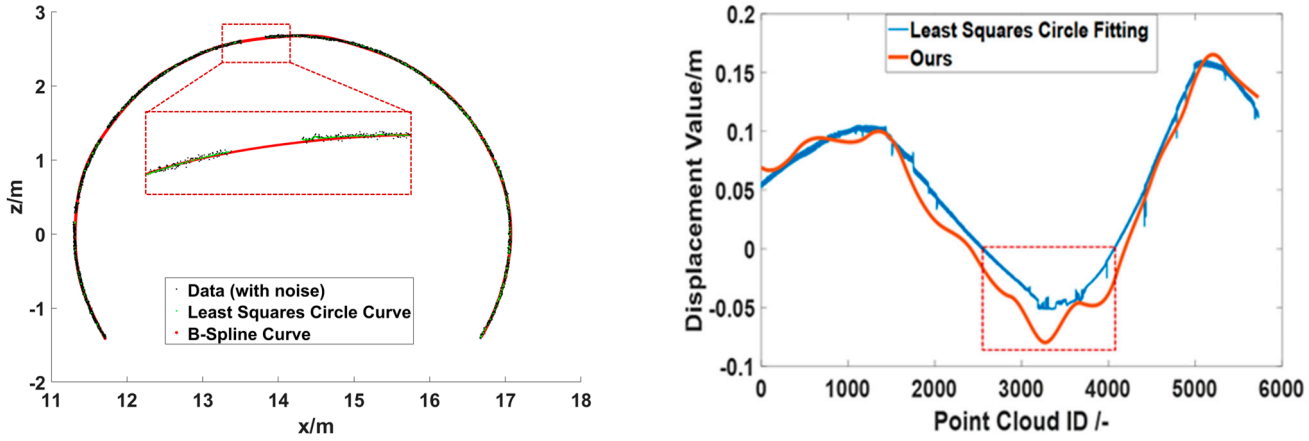
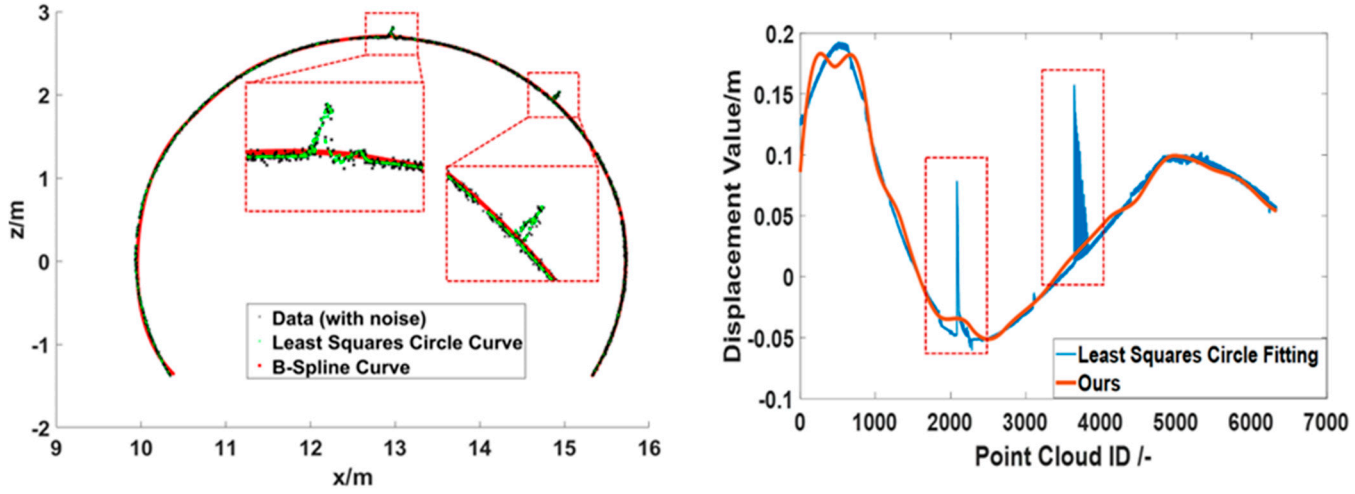


Figure 9. Multi-segment continuous point cloud missing for cross-section 2. (**a**) Fitted curve. (**b**) Point displacement.



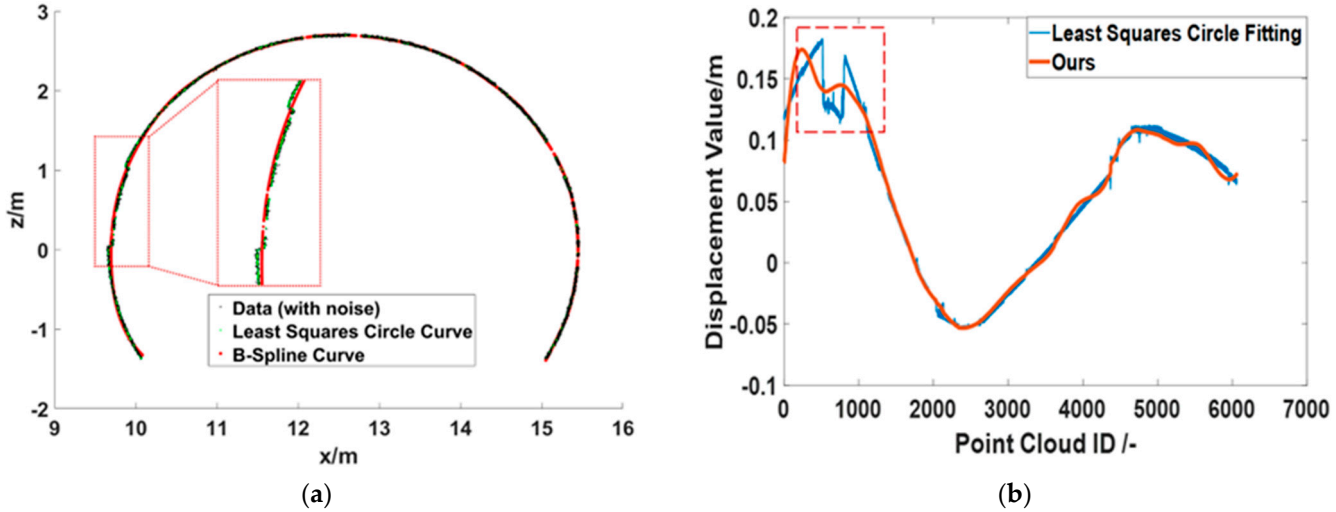
(**a**) (**b**)

Figure 10. Long-distance point cloud missing for cross-section 3. (**a**) Fitted curve. (**b**) Point displacement.



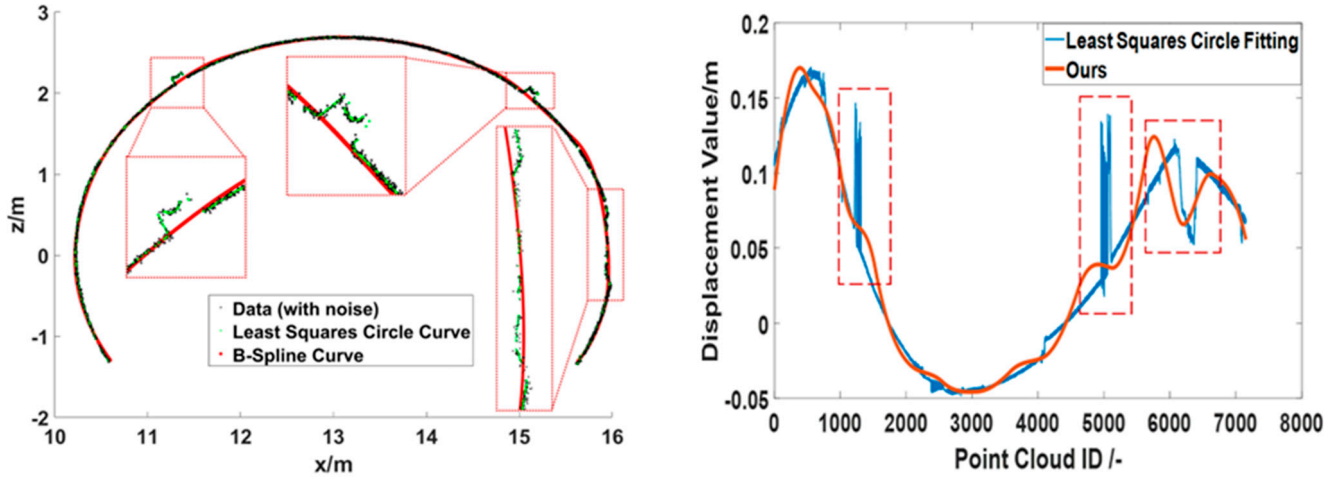
(**a**) (**b**)

Figure 11. Attachment outside the tunnel lining for cross-section 4. (**a**) Fitted curve. (**b**) Point displacement.



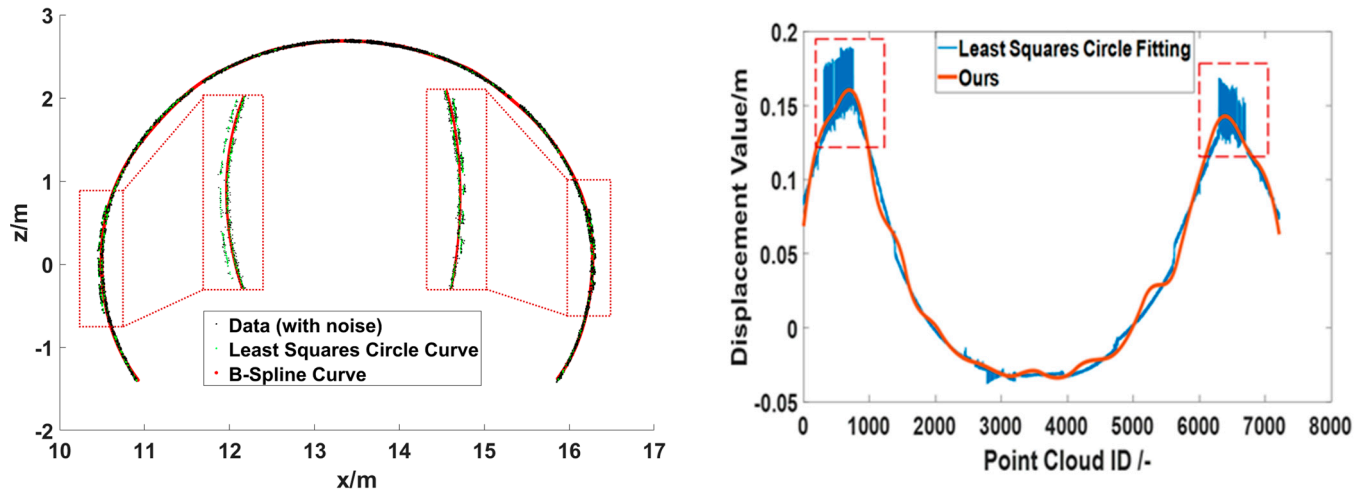
(**a**) (**b**)

Figure 12. Lining misplatforms for cross-section 5. (**a**) Fitted curve. (**b**) Point displacement.



(**a**) (**b**)

Figure 13. Attachment outside the tunnel lining and misplatforms for cross-section 6. (**a**) Fitted curve. (**b**) Point displacement.



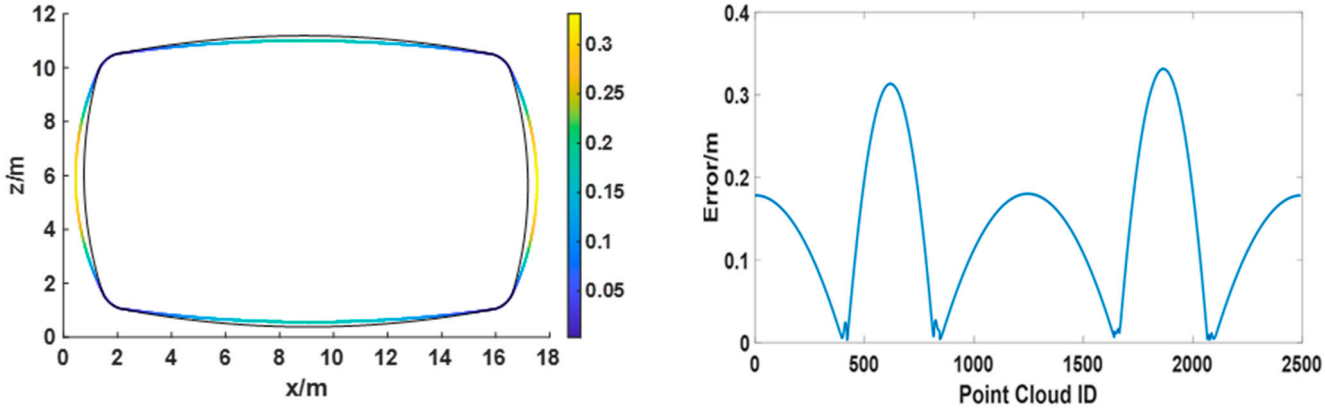
(**a**) (**b**)

Figure 14. Lining artefacts for cross-section 7. (**a**) Fitted curve. (**b**) Point displacement.

The robustness of our method regarding interference point clouds from lining outer appendages and the sensitivity to local deformation, such as tunnel lining misalignment, are again verified, as described above and shown in Figure 13. The lining artefacts are generated by the light when the 3D laser scanner collects the data, and the circle fitting algorithm will be affected by the artefacts when fitting the tunnel point cloud, thus showing concentrated up and down fluctuations in the converged deformation map, as shown in Figure 14. Our method can effectively identify the real position of the lining, and the curve trend is smoother in the convergent deformation map.

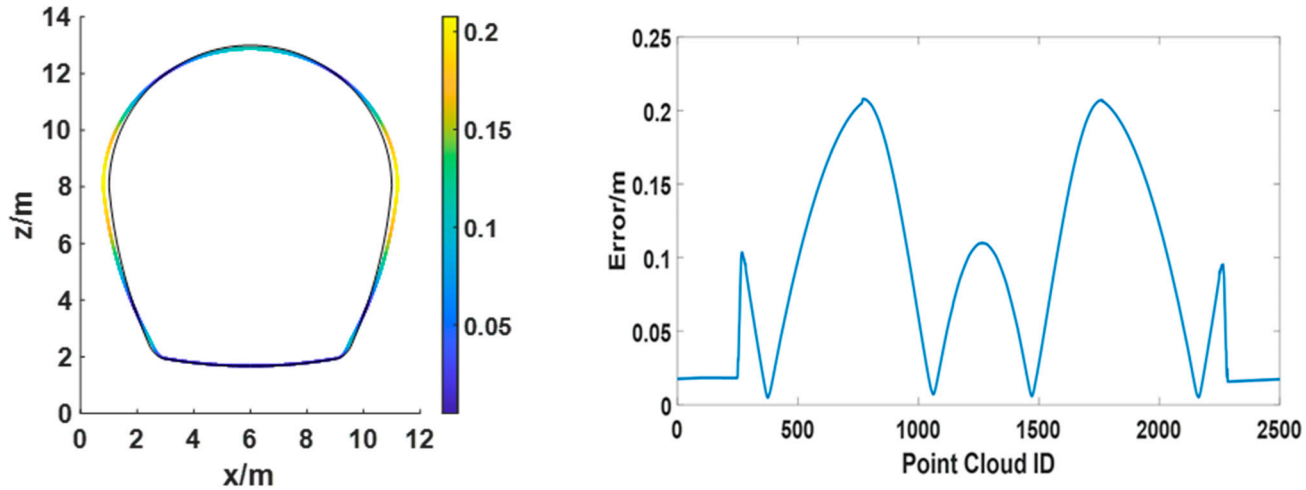
A rectangular-like tunnel and a horseshoe-shaped tunnel are modelled in computer-aided design to verify the applicability of our method. Then, we set the tunnel model rule for horizontal convergence and vault settlement, movement, and rotation to other coordinate positions. The models before and after the deformation of the tunnel in (a) can be accurately aligned, and the displacements of the points in (b) are consistent with the deformation characteristics of the rule, as shown in Figures 15 and 16. Our algorithm can be applied to various tunnel shapes as it iterates over the nearest-neighbor points and calculates the difference in distance between the corresponding points by curve transfor-

mation. The tunnel simulation model is limited in its inability to provide feedback on the real deformation, so it is discussed further after the field data is collected.



(**a**) (**b**)

Figure 15. Deformation analysis of a rectangular-like tunnel. (**a**) Visualization of color field deformation. (**b**) Point displacement.



(**a**) (**b**)

Figure 16. Deformation analysis of a horseshoe-shaped tunnel. (**a**) Visualization of color field deformation. (**b**) Point displacement.

5. Conclusions

Tunnel deformation analysis based on point cloud data is a cutting-edge and intelligent approach. It has high accuracy in tunnel deformation diagnosis, can effectively achieve normalized cycle monitoring of tunnel deformation, and save time and effort. Based on the principles of B-spline fitting and ICP alignment, this paper investigates a new method for tunnel convergence deformation monitoring with the following contributions:

1. A high-precision tunnel deformation monitoring method incorporating B-spline fitting and ICP alignment is proposed to monitor horizontal convergence, vault settlement and circumferential convergence with high accuracy.
2. Compared with the circle fitting algorithm, our method can automatically compensate for the missing point clouds, is not affected by the point clouds of the lining appendages inside and outside the tunnel, and is more sensitive concerning the feedback of local deformation.
3. The calculation of the difference between the radial distance and the design radius of a tunnel is transformed into a curve transformation that iterates over the nearest

neighbors and calculates the difference in the distance between the corresponding points; therefore, our method can be applied to a variety of tunnel shapes.

In the next stage of our work, we will continue to investigate ICP advanced algorithms based on extracting shape feature points to improve the accuracy of our method. We will dig deeper into other point cloud alignment algorithms, such as normal distribution point cloud alignment and point set alignment algorithms, to improve the adaptability of our method. In addition, we will compare the converged deformation results with the displacement field of the numerical model to invert the stress field of the tunnel lining and the stiffness of the tube joints and predict the subsequent deformation.

Author Contributions: Conceptualization, X.X.; Methodology, Z.W., X.X. and H.Y.; Formal analysis, Z.W.; Investigation, X.X., X.H., X.W. and H.Y.; Writing—original draft, Z.W.; Writing—review & editing, X.X., X.H., X.W. and H.Y.; Supervision, X.X.; Funding acquisition, X.H. All authors have read and agreed to the published version of the manuscript.

Funding: This research was funded by the Natural Science Foundation of China (No: 52308323, U1934209), Natural Science Foundation of Jiangsu Province, China (BK20220502) and Suzhou Innovation and Entrepreneurship Leading Talent Plan (No. ZXL2022488).

Data Availability Statement: The data provided in this work is available from the corresponding author.

Conflicts of Interest: The authors declare no conflict of interest.

References

1. Kaartinen, E.; Dunphy, K.; Sadhu, A. LiDAR-based structural health monitoring: Applications in civil infrastructure systems. *Sensors* **2022**, *22*, 4610. [CrossRef] [PubMed]
2. Luo, Y.B.; Chen, J.X.; Xi, W.Z.; Zhao, P.Y.; Qiao, X.; Deng, X.H.; Liu, Q. Analysis of tunnel displacement accuracy with total station. *Measurement* **2016**, *83*, 29–37. [CrossRef]
3. Yang, H.; Xu, X.Q.; Xu, X.Y.; Liu, W. TLS and FEM combined methods for deformation analysis of tunnel structures. *Mech. Adv. Mater. Struct.* **2022**, 1–8. [CrossRef]
4. Yang, H.; Xu, X.Y.; Kargoll, B.; Neumann, I. An automatic and intelligent optimal surface modeling method for composite tunnel structures. *Compos. Struct.* **2019**, *208*, 702–710. [CrossRef]
5. Puntu, J.M.; Chang, P.Y.; Lin, D.J.; Amania, H.H.; Doyoro, Y.G. A comprehensive evaluation for the tunnel conditions with ground penetrating radar measurements. *Remote Sens.* **2021**, *13*, 4250. [CrossRef]
6. Zhang, F.K.; Liu, B.; Liu, L.B.; Wang, J.; Lin, C.J.; Yang, L.; Li, Y.; Zhang, Q.S.; Yang, W.M. Application of ground penetrating radar to detect tunnel lining defects based on improved full waveform inversion and reverse time migration. *Near Surf. Geophys.* **2019**, *17*, 127–139. [CrossRef]
7. Hou, G.Y.; Li, Z.X.; Hu, Z.Y.; Feng, D.X.; Zhou, H.; Cheng, C. Method for tunnel cross-section deformation monitoring based on distributed fiber optic sensing and neural network. *Opt. Fiber Technol.* **2021**, *67*, 102704. [CrossRef]
8. Wang, T.; Shi, B.; Zhu, Y.H. Structural monitoring and performance assessment of shield tunnels during the operation period, based on distributed Optical-Fiber sensors. *Symmetry* **2019**, *11*, 940. [CrossRef]
9. Shen, F.X.; Song, Y.Q.; Zhao, W.C.; Wang, J.; Zheng, J.J.; Shao, Z.X. Experimental Study on Deformation Failure Mechanism of Surrounding Rocks for the Deep-Buried Twin Tunnels in Inclined Layered Strata During the Excavation. *Rock Mech. Rock Eng.* **2023**, *56*, 2311–2331. [CrossRef]
10. Meng, X.M.; Qi, T.J.; Zhao, Y.; Dijkstra, T.; Shi, W.; Luo, Y.F.; Wu, Y.Z.; Su, X.J.; Zhao, F.M.; Ma, J.H.; et al. Deformation of the Zhangjiazhuang high-speed railway tunnel: An analysis of causal mechanisms using geomorphological surveys and D-InSAR monitoring. *J. Mt. Sci.* **2021**, *18*, 1920–1936. [CrossRef]
11. Ai, Q.; Yuan, Y.; Bi, X.L. Acquiring sectional profile of metro tunnels using charge-coupled device cameras. *Struct. Infrastruct. Eng.* **2016**, *12*, 1065–1075. [CrossRef]
12. Xu, X.Y.; Kargoll, B.; Bureick, J.; Yang, H.; Alkhatib, H.; Neumann, I. TLS-based profile model analysis of major composite structures with robust B-spline method. *Compos. Struct.* **2018**, *184*, 814–820. [CrossRef]
13. Xu, X.Y.; Yang, H. Intelligent crack extraction and analysis for tunnel structures with terrestrial laser scanning measurement. *Adv. Mech. Eng.* **2019**, *11*, 1687814019872650. [CrossRef]
14. Xu, X.Y.; Yang, H. Robust model reconstruction for intelligent health monitoring of tunnel structures. *Int. J. Adv. Robot. Syst.* **2020**, *17*, 1729881420910836. [CrossRef]
15. Xu, X.Y.; Yang, H.; Kargoll, B. Robust and automatic modeling of tunnel structures based on terrestrial laser scanning measurement. *Int. J. Distrib. Sens. Netw.* **2019**, *15*, 1550147719884886. [CrossRef]

16. Farahani, B.V.; Barros, F.; Sousa, P.J.; Cacciari, P.P.; Tavares, P.J.; Futai, M.M.; Moreira, P. A coupled 3D laser scanning and digital image correlation system for geometry acquisition and deformation monitoring of a railway tunnel. *Tunn. Undergr. Space Technol.* **2019**, *91*, 102995. [CrossRef]
17. Cao, Z.; Chen, D.; Shi, Y.F.; Zhang, Z.X.; Jin, F.X.; Yun, T.; Xu, S.; Kang, Z.Z.; Zhang, L.Q. A flexible architecture for extracting metro tunnel cross sections from terrestrial laser scanning point clouds. *Remote Sens.* **2019**, *11*, 297. [CrossRef]
18. Feng, K.; He, C.; Qiu, Y.; Zhang, L.; Wang, W.; Xie, H.M.; Zhang, Y.Y.; Cao, S.Y. Full-scale tests on bending behavior of segmental joints for large underwater shield tunnels. *Tunn. Undergr. Space Technol.* **2018**, *75*, 100–116. [CrossRef]
19. Cao, Z.; Chen, D.; Peethambaran, J.J.; Zhang, Z.X.; Xia, S.B.; Zhang, L.Q. Tunnel reconstruction with block level precision by combining Data-Driven segmentation and Model-Driven assembly. *IEEE Trans. Geosci. Remote Sens.* **2021**, *59*, 8853–8872. [CrossRef]
20. Jia, D.F.; Zhang, W.P.; Liu, Y.P. Systematic Approach for Tunnel Deformation Monitoring with Terrestrial Laser Scanning. *Remote Sens.* **2021**, *13*, 3519. [CrossRef]
21. Xu, J.; Ding, L.Y.; Luo, H.B.; Chen, E.O.; Wei, L.C. Near real-time circular tunnel shield segment assembly quality inspection using point cloud data: A case study. *Tunn. Undergr. Space Technol.* **2019**, *91*, 102998. [CrossRef]
22. Xie, X.Y.; Zhao, M.R.; He, J.M.; Zhou, B. Automatic and Visual Processing Method of Non-Contact Monitoring for Circular Stormwater Sewage Tunnels Based on LiDAR Data. *Energies* **2019**, *12*, 1599. [CrossRef]
23. Yi, C.; Lu, D.N.; Xie, Q.; Xu, J.X.; Wang, J. Tunnel deformation inspection via global spatial axis extraction from 3D raw point cloud. *Sensors* **2020**, *20*, 6815. [CrossRef] [PubMed]
24. Xu, X.Y.; Yang, H.; Neumann, I. A feature extraction method for deformation analysis of large-scale composite structures based on TLS measurement. *Compos. Struct.* **2018**, *184*, 591–596. [CrossRef]
25. Kang, Z.Z.; Zhang, L.Q.; Tuo, L.; Wang, B.Q.; Chen, J.L. Continuous extraction of subway tunnel cross sections based on terrestrial point clouds. *Remote Sens.* **2014**, *6*, 857–879. [CrossRef]
26. Zhou, L.; Sun, G.X.; Li, Y.; Li, W.Q.; Su, Z.Y. Point cloud denoising review: From classical to deep learning-based approaches. *Graph. Models* **2022**, *121*, 101140. [CrossRef]
27. Cheng, Y.J.; Qiu, W.G.; Lei, J. Automatic extraction of tunnel lining cross-sections from terrestrial laser scanning point clouds. *Sensors* **2016**, *16*, 1648. [CrossRef]
28. Cui, H.; Ren, X.C.; Mao, Q.Z.; Hu, Q.W.; Wang, W. Shield subway tunnel deformation detection based on mobile laser scanning. *Autom. Constr.* **2019**, *106*, 102889. [CrossRef]
29. Wang, Z.H.; Shi, P.X.; Xu, X.Q.; Xu, X.Y.; Xie, F.; Yang, H. Automatic identification and intelligent optimization of tunnel-free curve reconfiguration. *Symmetry* **2022**, *14*, 2505. [CrossRef]
30. Xu, X.Y.; Yang, H.; Neumann, I. Time-efficient filtering method for three-dimensional point clouds data of tunnel structures. *Adv. Mech. Eng.* **2018**, *10*, 1687814018773159. [CrossRef]
31. Wroblewski, A.; Wodecki, J.; Trybala, P.; Zimroz, R. A method for large underground structures geometry evaluation based on multivariate parameterization and multidimensional analysis of point cloud data. *Energies* **2022**, *15*, 6302. [CrossRef]
32. Zhao, X.; Kargoll, B.; Omidalizarandi, M.; Xu, X.Y.; Alkhatib, H. Model selection for parametric surfaces approximating 3D point clouds for deformation analysis. *Remote Sens.* **2018**, *10*, 634. [CrossRef]
33. Du, L.M.; Zhong, R.F.; Sun, H.; Zhu, Q.; Zhang, Z. Study of the integration of the CNU-TS-1 mobile tunnel monitoring system. *Sensors* **2018**, *18*, 420. [CrossRef]
34. Sun, H.L.; Liu, S.; Zhong, R.F.; Du, L.M. Cross-Section deformation analysis and visualization of shield tunnel based on mobile tunnel monitoring system. *Sensors* **2020**, *20*, 1006. [CrossRef] [PubMed]
35. Du, L.M.; Zhong, R.F.; Sun, H.L.; Liu, Y.J.; Wu, Q. Cross-section positioning based on a dynamic MLS tunnel monitoring system. *Photogramm. Rec.* **2019**, *34*, 244–265. [CrossRef]
36. Cox, M. The numerical evaluation of B-splines. *IMA J. Appl. Math.* **1972**, *10*, 134–149. [CrossRef]
37. De Boor, C. On calculating with B-splines. *J. Approx. Theory* **1972**, *6*, 50–62. [CrossRef]
38. Piegl, L.; Tiller, W. *The NURBS Book*; Springer Science & Business Media: Berlin, Germany, 1997.
39. Farin, G.E. *Curves and Surfaces for CAGD: A Practical Guide*; Morgan Kaufmann: Burlington, MA, USA, 2002.
40. Bureick, J.; Neuner, H.; Harmening, C.; Neumann, I. Curve and Surface Approximation of 3D Point Clouds. *Allg. Vermess. Nachr.* **2016**, *123*, 315–327.
41. Xu, X.Y.; Wang, Z.H.; Shi, P.X.; Liu, W.; Tang, Q.; Bao, X.H.; Chen, X.S.; Yang, H. Intelligent monitoring and residual analysis of tunnel point cloud data based on free-form approximation. *Mech. Adv. Mater. Struct.* **2023**, *30*, 1703–1712. [CrossRef]
42. Besl, P.J.; McKay, N.D. A method for registration of 3D shapes. *IEEE Trans. Pattern Anal. Mach. Intell.* **1992**, *14*, 239–256. [CrossRef]
43. Zhao, Y.; Zhu, Z.Z.; Liu, W.; Zhan, J.Y.; Wu, D. Application of 3D laser scanning on NATM tunnel deformation measurement during construction. *Acta Geotech.* **2023**, *18*, 483–494. [CrossRef]

Disclaimer/Publisher's Note: The statements, opinions and data contained in all publications are solely those of the individual author(s) and contributor(s) and not of MDPI and/or the editor(s). MDPI and/or the editor(s) disclaim responsibility for any injury to people or property resulting from any ideas, methods, instructions or products referred to in the content.